Timing of ESCRT-III protein recruitment and membrane scission during HIV-1 assembly

Daniel S. Johnson[1,2], Marina Bleck[1], Sanford M. Simon[1]

[1]Laboratory of Cellular Biophysics, The Rockefeller University, New York, NY 10065, USA
[2]Department of Physics and Astronomy, Hofstra University, Hempstead, NY 11549, USA

The Endosomal Sorting Complexes Required for Transport III (ESCRT-III) proteins are critical for cellular membrane scission processes with topologies inverted relative to clathrin-mediated endocytosis. Some viruses appropriate ESCRT-IIIs for their release. By imaging single assembling viral-like particles of HIV-1, we observed that ESCRT-IIIs and the ATPase VPS4 arrive after most of the virion membrane is bent, linger for tens of seconds, and depart ~20 seconds before scission. These observations suggest ESCRT-IIIs are recruited by a combination of membrane curvature and the late domains of the HIV-1 Gag protein. ESCRT-IIIs may pull the neck into a narrower form but must leave to allow scission. If scission does not occur within minutes of ESCRT departure, ESCRT-III and VPS4 are recruited again. This mechanistic insight is likely relevant for other ESCRT dependent scission processes including cell division, endosome tubulation, multivesicular body and nuclear envelope formation, and secretion of exosomes and ectosomes.

Introduction

ESCRTs are categorized into groups -0 through -III and act in various cellular processes including cell division, multivesicular body formation, and wound repair (Hurley, 2015). An investigation of protein sorting between endosomes and lysosomes initially led to the discovery of ESCRT-I (Katzmann et al., 2001), with other ESCRTs identified soon afterwards (Babst et al., 2002a; Babst et al., 2002b; Katzmann et al., 2003). Sequential recruitment of the ESCRTs enables division of membrane compartments, with ESCRT-III being critical for the membrane scission process (Henne et al., 2013). ESCRT-IIIs have a five alpha-helix core structure and assemble *in vitro* into macromolecular rings or spirals (McCullough et al., 2015; Muziol et al., 2006). ESCRT-IIIs are believed to polymerize in the neck of the membrane constriction to drive membrane fission (Cashikar et al., 2014; Dobro et al., 2013; Fabrikant et al., 2009; Hanson et al., 2008; Henne et al., 2012; Lata et al., 2008; McCullough et al., 2015).

Scission of the membrane, even in the presence of ESCRT-IIIs, stalls in the absence of the hexameric AAA^+ ATPase (Morita et al., 2010), VPS4A/B, which contains a microtubule interacting and transport (MIT) domain that binds to MIT interacting motifs (MIM) of ESCRT-IIIs (Obita et al., 2007; Stuchell-Brereton et al., 2007). The final scission process is believed to be associated with VPS4 working on ESCRT-IIIs, but the mechanism is still unresolved. In some models the ESCRT-IIIs provide the motive force for scission and the VPS4 is required after scission to recycle the ESCRT-IIIs for subsequent scissions (Lata et al., 2008; Wollert et al., 2009). In other models the VPS4 is actively engaging the ESCRT-IIIs prior or during scission by actively remodeling ESCRT-IIIs in order to force scission (Saksena et al., 2009), by rearranging ESCRT-IIIs as part of the pathway towards scission (Cashikar et al., 2014), or by binding to ESCRT dome structures in order to add rigidity necessary for scission (Fabrikant et al., 2009).

ESCRT complexes are hijacked by HIV to enable separation of the viral particle from the host cell plasma membrane. The production of enveloped HIV-1 at the plasma membrane occurs with the recruitment of the structural protein Gag at individual assembly sites. The carboxyl terminus of Gag has a motif that is essential for recruitment of ESCRTs. First Gag recruits the "early" ESCRTs which contribute to subsequent recruitment of ESCRT-III proteins. The ESCRT-IIIs then polymerize into structures that are believed to constrict the neck and drive membrane fission. HIV release appears to require fewer members of the ESCRT family than other processes. Redundancy likely makes many variants, such as CHMP5, CHMP6 and CHMP7, only conditionally necessary (Morita et al., 2011). ESCRT-IIIs that are essential for assembly of HIV-1 include CHMP2 (either A or B variant) and CHMP4B, which are recruited to site of budding with other proteins such as ALIX and TSG101 which interact with Gag (Morita et al., 2011). The reduced number of required ESCRTs makes HIV assembly an approachable system for studying the biophysics of ESCRT mediated membrane scission.

Prior to viral particle separation from a host cell, a roughly spherical particle is formed (Martin-Serrano et al., 2003), but the topological pathway and timing of events to reaching the Gag sphere has not previously been followed *in vivo*. The order of some of the events in virion assembly has been resolved by live-cell microscopy. First the HIV- genome is recruited to the membrane, potentially with a few Gag molecules (Jouvenet et al., 2009). Then, over a 5-30 minute period, the Gag accumulates around the genome (Ivanchenko et al., 2009; Jouvenet et al., 2008). Once Gag reaches a steady-state, ESCRT-III and VPS4 are transiently recruited at the site of assembly (Baumgartel et al., 2011; Bleck et al., 2014; Jouvenet et al., 2011). The timing of some critical steps is not known impacting our understanding of the mechanism. It is not known whether bending occurs before, during, or after the transient recruitment of ESCRTs. Thus, is membrane bending driven by Gag multimerization, by Gag engagement with the HIV-1 genome or by the ESCRTs? It is also not known if scission occurs before, during or after the transient recruitment of ESCRT-IIIs or VPS4. Do they generate the force for scission, do they prepare the membrane for scission, or does VPS4 recycle ESCRT-IIIs after scission?

Here we investigated, during the assembly of HIV Gag, the temporal recruitment of ESCRT-III proteins and VPS4 relative to membrane scission. We also examined membrane curvature during Gag assembly to determine when a spherical particle forms relative to ESCRT-III recruitment. We find that membrane bending occurs contemporaneous with recruitment of Gag and prior to arrival ESCRT-III. The ESCRT-IIIs and the VPS4 ATPase arrive after Gag assembly has concluded, remain at the membrane for tens of seconds, and then leave tens of seconds before scission. During the period after departure of the ESCRT-IIIs, neutralizing the surface charge on the membrane accelerates the membrane scission.

Results

ESCRT-IIIs appear and disappear from site of virus-like particle assembly prior to scission.

To determine the timing of ESCRT recruitment relative to membrane bending and scission, we quantified ESCRT recruitment during the assembly of HIV-1 virus like particles (VLPs) while assaying membrane bending and scission. Scission was assayed by monitoring the ability of protons to flow between the cytosol and the lumen of the virion. The pH in the lumen of the virion was monitored with a pH-sensitive GFP (pHlourin) (Miesenbock et al., 1998) fused

to Gag (Jouvenet et al., 2008) while modulating the cytoplasmic pH by cycling the pCO_2 every 10 s between 0% and 10%, thus an average of 5% pCO_2 (Figure 1 – figure supplement 1). CO_2 rapidly diffuses across plasma membranes (Hulikova and Swietach, 2014; Simon et al., 1994) and is converted to carbonic acid by cytoplasmic carbonic anhydrase, altering the cytoplasmic pH. We have previously observed that Gag-pHlourin in a budded VLP is less sensitive to changes of pCO_2 than in the cytosol, suggesting carbonic anhydrase is excluded from VLPs (Jouvenet et al., 2008).

At sites of VLP assembly the average Gag-pHluorin fluorescence increase was similar to the increase of Gag-mEGFP (Jouvenet et al., 2008), but the intensity oscillated in sync with switching the pCO_2 (Figure 1A, Figure 1 – figure supplement 2). At various times after Gag accumulation reached a steady-state maximum the magnitude of oscillations decreased, indicating a loss of the ability of protons to move between the VLP and cytoplasm due to scission. Not surprisingly, scission was never observed before Gag had finished accumulating at individual VLPs. Unexpectedly the ESCRT-III CHMP4B both appeared (Avg=59s, N=30 out of 30) and disappeared (Avg=22s, N=27 out of 30) prior to scission (Figure 1B).

CHMP4B has been proposed to form a circular/spiral structure which supports assembly of a smaller CHMP2(A/B) dome which generates fission by pulling the neck together (Fabrikant et al., 2009). Thus, it is possible that CHMP4B may be removed prior to scission leaving CHMP2A or CHMP2B present to facilitate fission. To probe the timing of CHMP2, endogenous CHMP2A and CHMP2B were lowered with siRNA (Figure 1 – figure supplement 3) to facilitate observation of mCherry-CHMP2A or mCherry-CHMP2B (Figure 1C and E, Figure 1 – figure supplement 2). CHMP2A and CHMP2B both appeared (Avg.=77s, N=29 out of 29; and 63s, N=23 out of 23, respectively) and disappeared prior to scission (Avg. = 23s, N=26 out of 29; and 27s, N=23 out of 23, respectively Figure 1D,F). This observation indicates their assembly and disassembly is also not physically forcing scission.

Next the dynamics of recruitment of VPS4, the energy providing ATPase, was monitored (Figure 1G and Figure 1 – figure supplement 2). Similar to the ESCRT-IIIs, VPS4A also appeared prior to scission (Avg=42s, N=28 out of 28) and disappeared prior to scission (Avg=17s, N=27 out of 28, Figure 1H). On average VPS4A disappeared from the assembly site closer to the time of scission than CHMP4B (5 s), CHMP2A (6 s) or CHMP2B (10 s). A simultaneous measurement of CHMP4B and VPS4A confirmed CHMP4B was recruited ~5 s prior to VPS4A (N=41) (Figure 1 – figure supplement 4), which agrees with previous results in HeLa cells (Bleck et al., 2014).

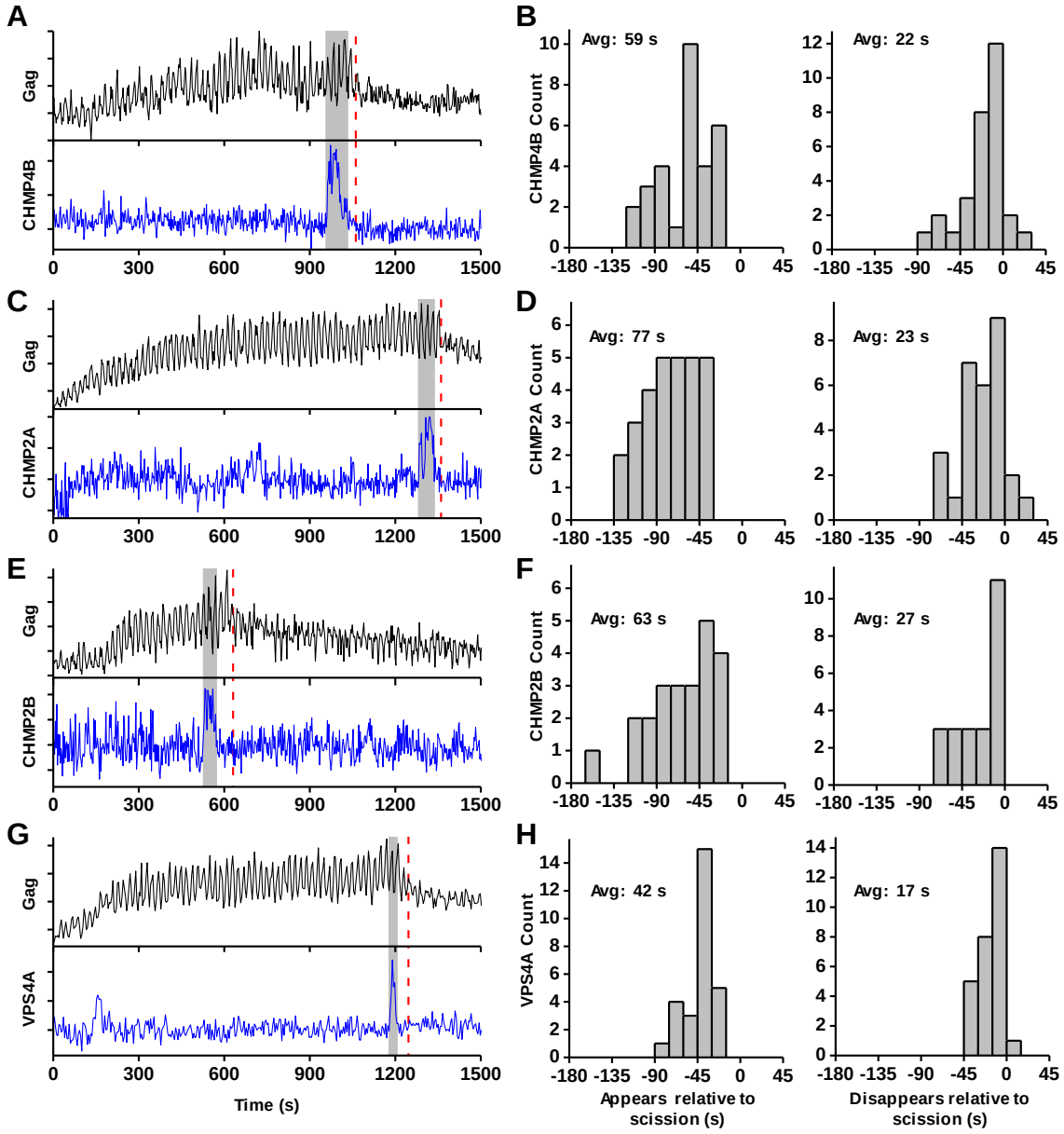

Figure 1. ESCRT-IIIs and VPS4A transiently recruited prior to scission. (**A**) Example trace of Gag-pHluorin assembling into single VLP while the pCO_2 in the imaging media was repeatedly switched between 0% and 10% every 10 s. Moment of scission is indicated by red dashed line. CHMP4B-mCherry was temporarily recruited (indicated by grey zone) to the site of VLP assembly following the loss of pH modulation sensitivity. (**B**) Histograms of appearance and disappearance of CHMP4B prior to scission. (**C-H**) Example traces and histograms of appearance and disappearance, relative to scission of the VLP, for mCherry-CHMP2A (C and D), mCherry-CHMP2B (E and F) and mCherry-VPS4A (G and H).

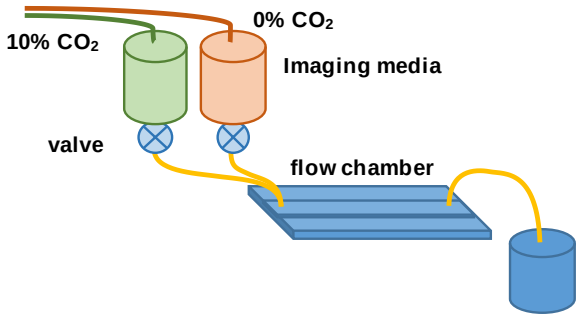

Figure 1 – figure supplement 1. Flow chamber configuration for ESCRT-III assisted membrane scission studies. Imaging media in reservoirs was preequilibrated with gas containing 0% and 10% CO_2 (balanced with air). During assembly of single HIV particles in cells the imaging media was modulated between reservoirs, enabling detection of scission of the VLP from the cell.

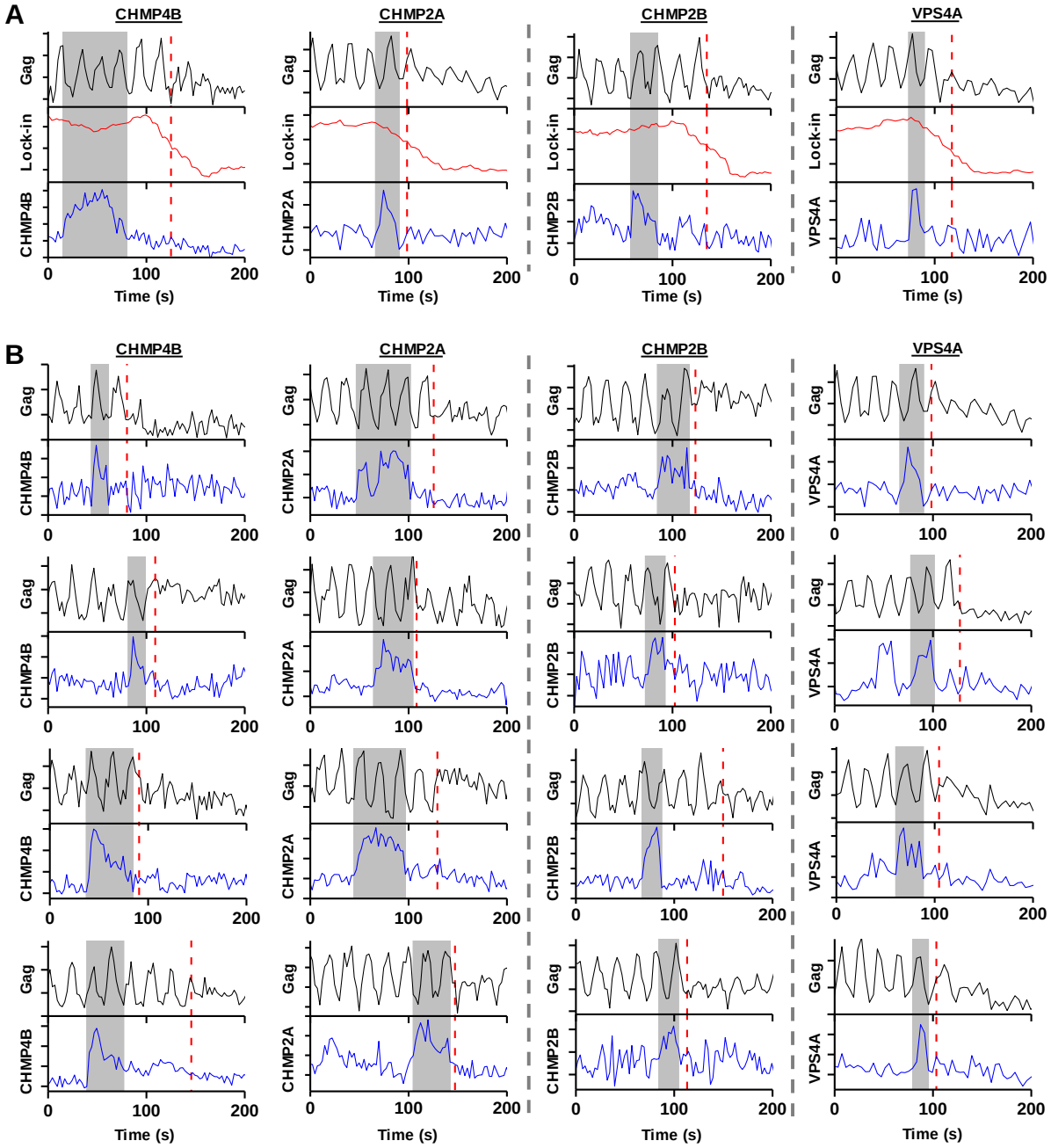

Figure 1 – figure supplement 2. Example traces of scission relative to recruitment of ESCRT-III or VPS4A. (**A**) Gag-pHluorin was observed as pCO_2 was cycled between 0% and 10% every 10 s. VLP scission time (red dashed line) was characterized by half drop in lock-in signal. mCherry-CHMP4B, mCherry-CHMP2A, mCherry-CHMP2B and mCherry-VPS4A recruitment (left to right panels, recruitment highlighted in grey) were simultaneously monitored during Gag assembly. (**B**) Additional traces of VLP scission during recruitment of mCherry-CHMP4B, mCherry-CHMP2A, mCherry-CHMP2B, and mCherry-VPS4A (left to right columns).

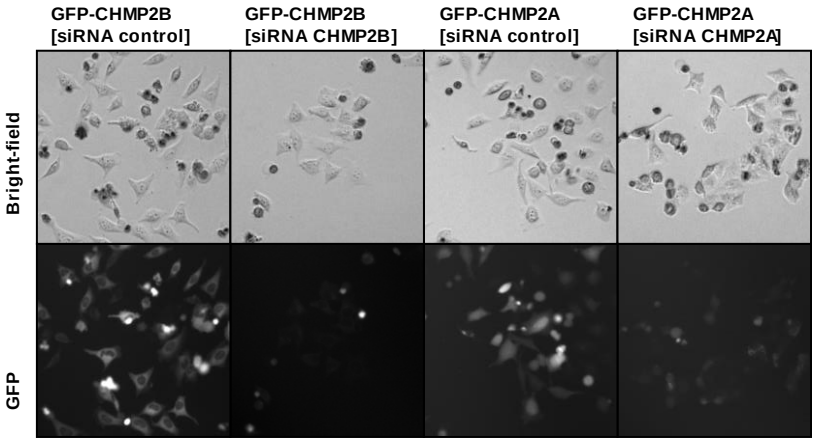

Figure 1 – figure supplement 3. Knockdown of CHMP2A or CHMP2B by siRNA. HeLa cell lines stably expressing either mEGFP-CHMP2A or mEGFP-CHMP2B were transfected with siRNA to either CHMP2A or CHMP2B or a control siRNA. 48 hours after transfection, presence of tagged ESCRT was significantly reduced and resulted in fewer cells, presumably because of decreased cell division.

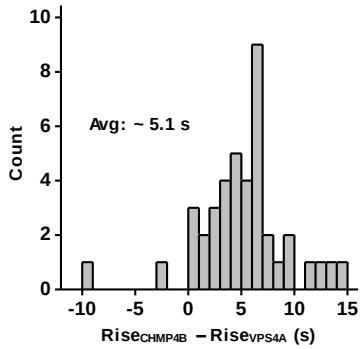

Figure 1 – figure supplement 4. CHMP4B was recruited prior to VPS4A. The times associated with the rising fluorescence edge of VPS4A and CHMP4B were compared relative to each other. CHMP4B appeared on average 5.1 s prior to VPS4A.

Acidification of cytosol accelerates scission

Our results indicate that the ESCRT-IIIs and the ATPase VPS4 leave the membrane prior to scission. It is possible that the ESCRT-IIIs play an essential role in tightening the membrane neck, but then need to be cleared away to allow for the opposing membranes to come closer for the scission reaction. The specific lipid composition in the neck is not known. However, both HIV-1 Gag and the ESCRT complexes are recruited to regions rich in phosphatidylinositol 4,5-bisphosphate (PIP_2), which has four negative charges at pH 7 (Kooijman et al., 2009), with the net negative charge being the critical parameter for engaging ESCRTs (Lee et al., 2015). Thus, ESCRTs at the neck may bias the composition towards more negatively charged lipids (Chiaruttini et al., 2015). The pKa values for the two phosphate groups on the PI of PIP_2 are 6.5 and 7.7 (van Paridon et al., 1986). Lowering the pH by raising the pCO_2 to 10% should protonate and thus reduce the charge of these negatively charged lipids thus reducing the repulsive force between the membranes. To test if scission was affected by the changes in cytosolic pH we switched the pCO_2 at a slower rate, every 120s (Figure 2). Scission was ~ 3X more likely when the cytoplasm was in the low pH state (10% pCO_2) than the high pH state (0% pCO_2) (Figure 2F) consistent with the idea that scission is more likely when the net negative charge on phospholipids in the viral neck is reduced by protonation.

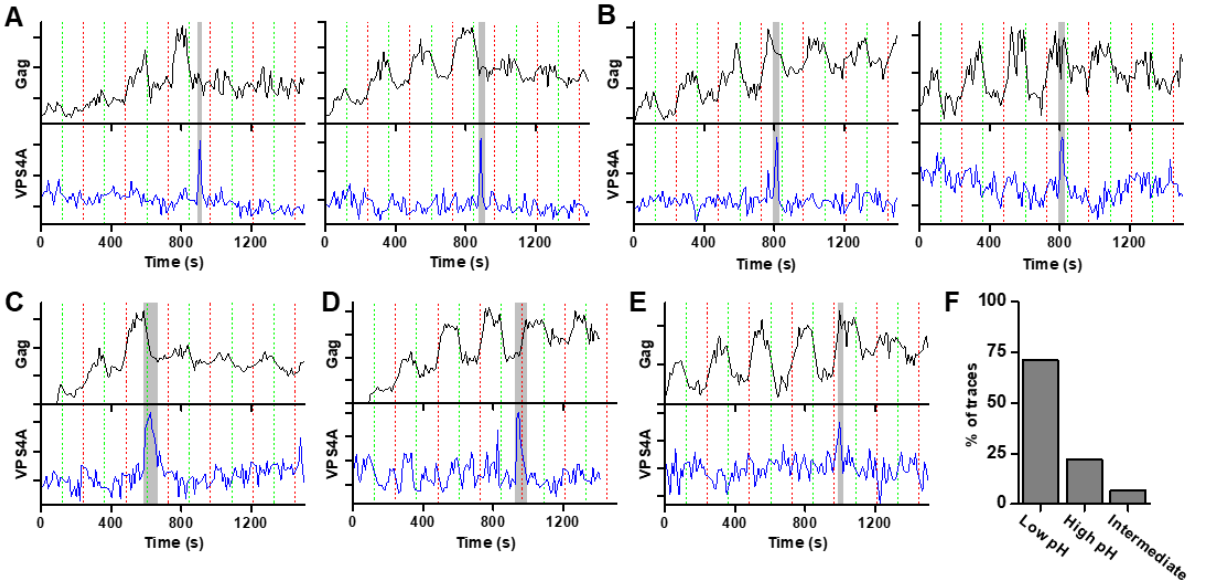

Figure 2. Scission more likely at lower cytoplasmic pH. (**A**) Example traces of Gag-pHluorin assembly while pCO_2 was switched every 120s between 0% (red dashed line, greater fluorescence emission) and 10% (green dashed line, lower fluorescence emission). In these traces the fluorescence intensity became fixed in the low pH state (10% pCO_2) after reaching an assembly plateau. VPS4A appeared and disappeared during the first low pH state. (**B**) Examples in which fluorescence intensity became fixed in the high pH state (0% pCO_2). VPS4A appeared and disappeared during the first trapped high pH state. (**C**) Example in which fluorescence became fixed in low pH state. VPS4A disappeared during the first trapped low pH state, but appeared during the previous high pH state. (**D**) Example in which fluorescence became fixed in high pH state. VPS4A disappeared during the first trapped high pH state, but appeared during the previous low pH state. (**E**) Example trace in which fluorescence intensity because fixed in a middle state. VPS4A disappeared near the time of transition. (**F**) Bar graph of cytoplasmic pH condition in which scission occurs (N=45). Scission is ~ 3-fold more likely at low pH (10%

186 pCO_2) compared to high pH (0% pCO_2) condition. A small percentage of VLPs were trapped in
187 an intermediate state.

188 **Additional rounds of ESCRT-III/VPS4 recruitment occur following failed scission**

189 Multiple rounds of ESCRT-III/VPS4 recruitment were previously observed following
190 completion of Gag accumulation (Baumgartel et al., 2011; Jouvenet et al., 2011). It is possible
191 the first wave of ESCRT-III/VPS4 led to productive scission and the subsequent rounds are
192 inconsequential. Alternatively, the initial waves could be non-productive, perhaps a consequence
193 of a failure to recruit both ESCRT-IIIs and VPS4A concurrently, necessitating additional rounds.
194 While simultaneously imaging Gag-pHluorin, CHMP4B and VPS4A, when there were multiple
195 waves, both CHMP4B and VPS4 were recruited (Figure 3). Scission was only observed after the
196 final wave of recruitment of ESCRT-III/VPS4 (Figure 3 B,C). Thus, not every cycle of arrival
197 and then dispersal of ESCRT-III/VPS4 leads to subsequent scission. If scission does not occur,
198 then a subsequent cycle of recruitment and dispersal of the ESCRT-III/VPS4 is required to
199 complete the process. If the function of VPS4A is to recycle ESCRT-IIIs after scission, then only
200 a single wave would be expected since ESCRT-IIIs would not be removed until after the single
201 scission event has occurred.

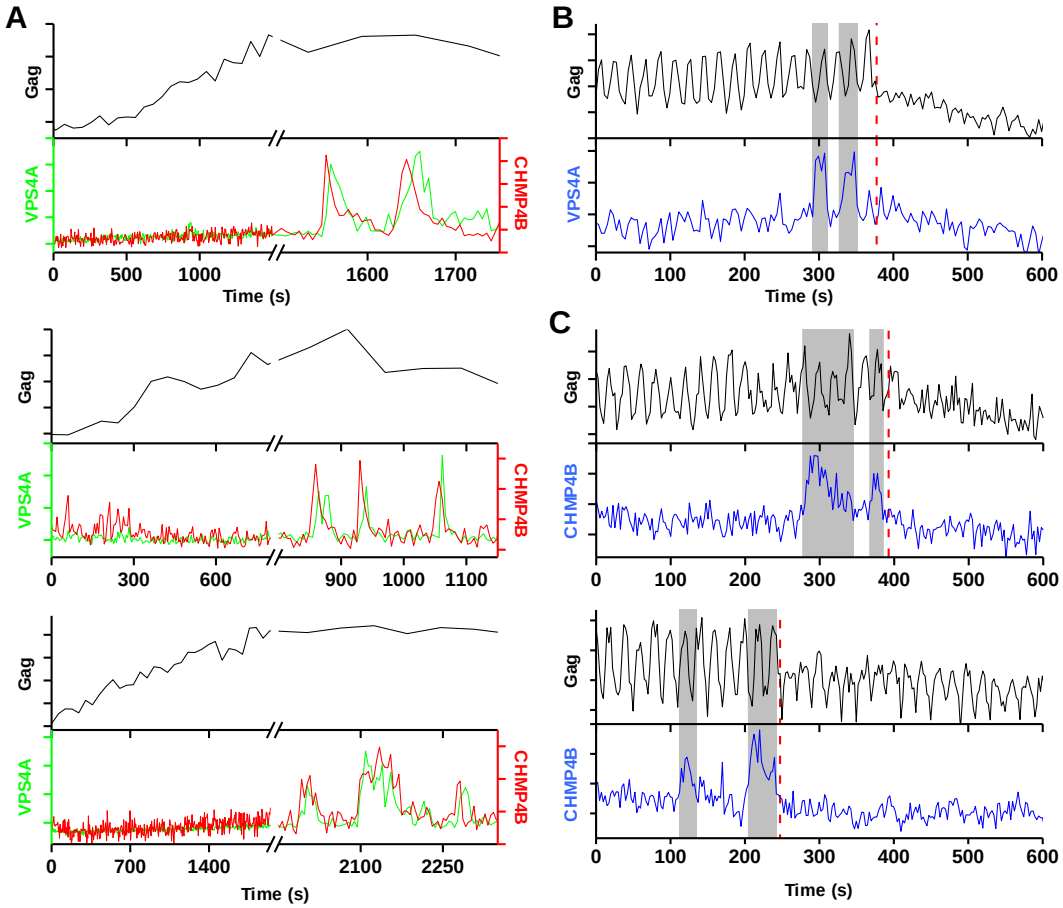

202
203 **Figure 3.** A new round of ESCRT-III recruitment required following failed scission event. (**A**)
204 Example trace of multiple waves of VPS4A and CHMP4B recruited following cessation of Gag
205 accumulation. (**B**) Example trace of multiple recruitments of VPS4A prior to scission (red

dashed line). (**C**) Example traces of multiple recruitments of CHMP4B prior to scission (red dashed line).

Membrane bending occurs throughout assembly of virus-like particle.

Next, we set out to determine when membrane bending occurs relative to the assembly of Gag and recruitment of ESCRT-IIIs. We expressed a fluorescent protein (either EGFP or one of two circularly permutated superfolder variants, sf3 or sf11 (Pedelacq et al., 2006)) as a fusion to Gag (at the carboxyl terminus or in the matrix protein of Gag) to be able to follow membrane bending in live-cell imaging via changes in anisotropy of the GFP tag.

The orientation of the chromophore was characterized with a custom built polarized total internal reflection fluorescence (TIRF) illuminator (Johnson et al., 2014). During accumulation of Gag at VLPs, the emission of the GFP was quantified while excitation alternated with polarization perpendicular ($\hat{\mathbf{p}}$ polarized) followed by parallel ($\hat{\mathbf{s}}$ polarized) to the glass surface. Orientation was characterized by the ratio of emission intensities (P/S) and total Gag was monitored by P + 2S (Figure 4A and Figure 4 – supplement figure 1) (Anantharam et al., 2010). As Gag accumulated, the ratio of P/S dropped from ~2 to ~1.4, with little variation (± 0.1) between the Gag-GFP versions (Figure 4B). The drop in P/S correlated with the increase in Gag as would be expected if the plasma membrane was bending during Gag assembly. The halfway decrease of P/S occurred prior to the halfway increase of the total Gag fluorescence (Figure 4C). Following Gag recruitment, as indicated by a plateau in Gag signal, there was no transition in P/S. This observation is inconsistent with the subsequent recruitment of the ESCRT-IIIs facilitating the transition from a flat lattice to a spherical particle.

A simulation of spherical budding reproduced the time course of the P/S ratio relative to P + 2S

In order to better understand the observed P/S ratio we formulated an expected P/S ratio for a spherical cap growing out of a flat membrane (Figure 4D). Briefly, we assumed the growing bud consisted of excitation dipoles uniformly distributed across the surface, with the dipoles oriented an angle β relative to the surface normal. A predicted P/S with respect to β and the normalized budded surface area (area from 0 to 1) was then found by integrating over all defined dipole orientations and the extent budded surface area.

More specifically, using coordinates described previously (Anantharam et al., 2010), position on the surface of the sphere was given in terms of a polar angle θ and an azimuthal angle ϕ, and the current extent budded was defined by θ (Figure 4E). Thus, when $\theta = 0^\circ$ there was no budding, when $\theta = 90^\circ$ the sphere was half budded with dipoles from $\theta = 0^\circ \rightarrow 90^\circ$, and when $\theta = 180^\circ$ the sphere was fully budded with dipoles from $\theta = 0^\circ \rightarrow 180^\circ$. A uniform distribution of excitation dipoles was assumed on the bud (no dependence on ϕ or θ); however, at any given position these dipoles had an angular distribution that depended on the polar angle β relative to the surface normal: $\rho(\beta)$. For instance, if all dipoles were oriented at $\beta = 45^\circ$ then $\rho(\beta) = \delta(\beta - 45^\circ)$ where $\delta(x)$ is a delta function. The angular distribution was assumed to be uniform relative to the surface azimuthal angle ψ and the sphere was assumed to be smaller than the optical resolution of the microscope.

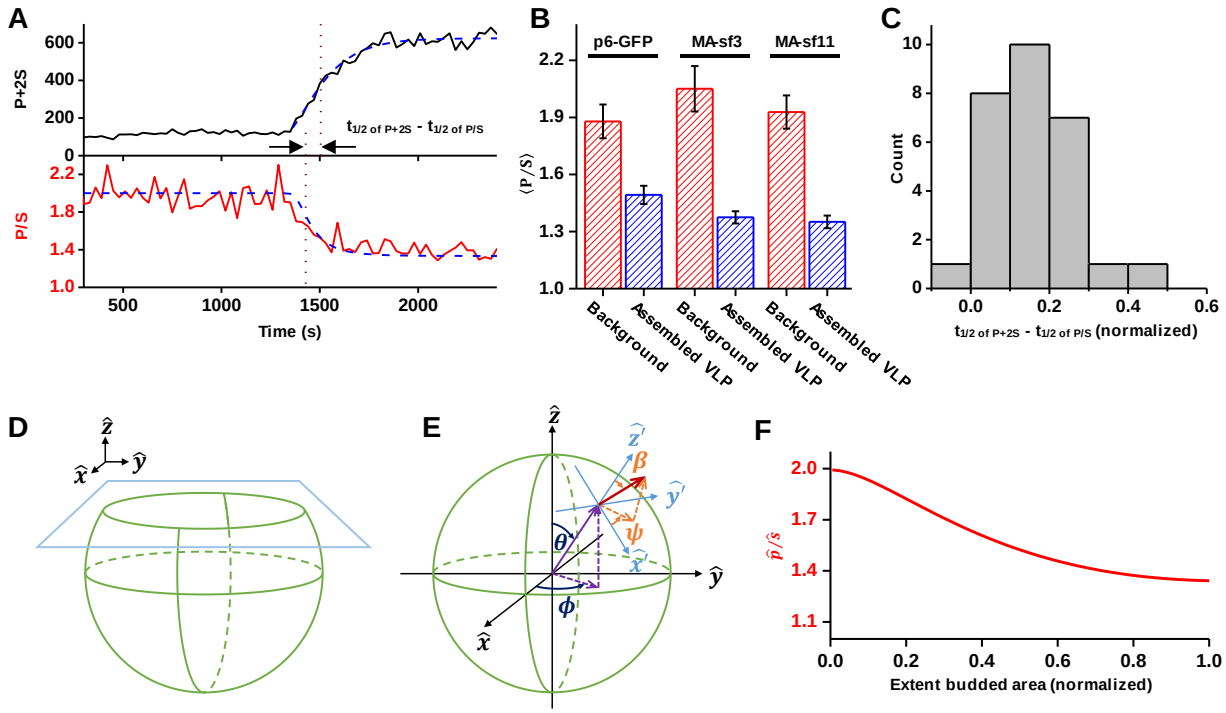

Figure 4. Structural changes in VLPs throughout Gag accumulation. (**A**) Example trace of Gag-GFP (sf3 in Matrix of Gag) assembling into a single VLP. Images were collected every 30 s with excitation illumination polarized either perpendicular ($\hat{\mathbf{p}}$) or parallel ($\hat{\mathbf{s}}$) to the glass surface. Total Gag characterized by P + 2S (black line) and relative average dipole orientation by P/S (red line). P + 2S was fit to an exponential and used to predict an expected P/S (blue dashed line) assuming membrane bending throughout assembly. (**B**) Comparison of average P/S from all traces before VLP assembly (membrane background) and after VLP assembly (plateau region) for three different tagged versions of Gag. p6-GFP (N=8), MA-sf3 (N=9), and MA-sf11 (N=7). Error bars represent s.d. (**C**) To compare the evolution of VLP structure to the assembly of Gag the time for each assembly trace was normalized from 0 (beginning of Gag assembly) to 1 (end of Gag assembly). A normalized time difference for each trace between Gag half assembly [½ $(P + 2S)_{max}$] and the dipole half drop [½ $(P/S)_{max}$] was found and all normalized differences were compiled into histogram. (**D**) Illustration of sphere budding from flat membrane with extent budded represented by θ. (**E**) Illustration of coordinate system with θ and ϕ representing position on the sphere and β and ψ representing orientation of excitation dipole. (**F**) Predicted P/S when $\beta = 45^{\circ}$, background intensity is 45% of full assembly intensity, and evanescent field penetration depth is the same as the radius of the VLP.

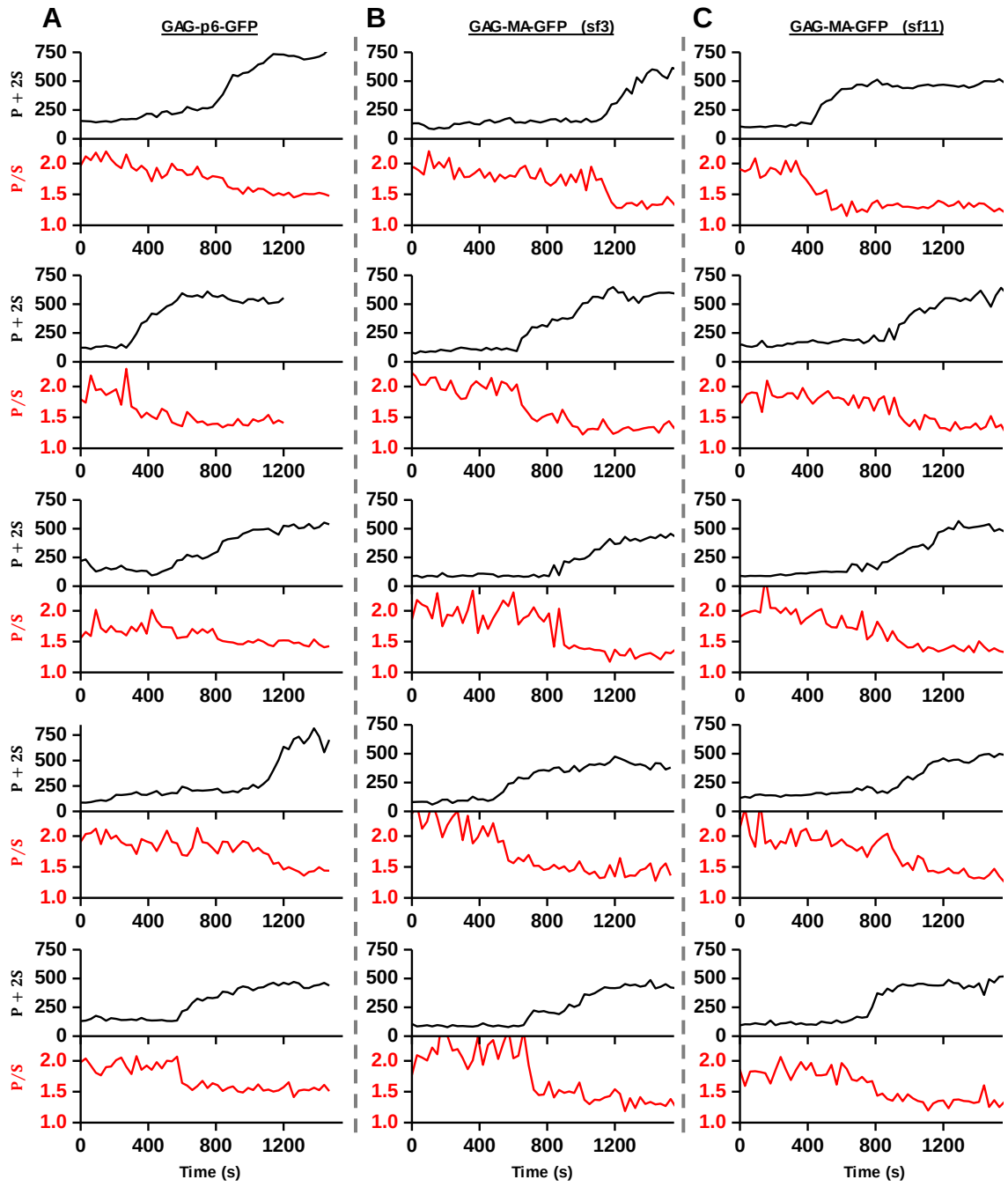

Figure 4 – figure supplement 1. Example traces of Gag accumulation (quantified as P + 2S) and fluorophore polarization (quantified as P/S) during VLP assembly. Three different tagging schemes were used: labeled with mEGFP after p6 domain at carboxy terminal of Gag (**A**), labeled with circularly permutated GFP variant 3 in matrix of Gag (**B**), labeled with circularly permutated GFP variant 11 in matrix of Gag (Pedelacq et al., 2006) (**C**).

A predicted $P/S\,(\rho(\beta))$ relative to extent budded θ was found by determining the average component of the dipole excitation in $\hat{\mathbf{y}}$ (parallel to glass surface) and in $\hat{\mathbf{z}}$ (normal to glass surface). Note: Experimentally due to azimuthal scanning we excited in both $\hat{\mathbf{x}}$ and $\hat{\mathbf{y}}$, each 50% the time, but for simplicity in this analysis 100% excitation in $\hat{\mathbf{y}}$ was assumed since $\hat{\mathbf{x}}$ and $\hat{\mathbf{y}}$ are symmetric. The total collected fluorescence, S and P, in $\hat{\mathbf{y}}$ and $\hat{\mathbf{z}}$ were predicated by:

$$S = \int_0^{\theta}\int_0^{2\pi}\int_0^{\pi}\int_0^{2\pi} Q_{\parallel}\left|E_{\hat{\mathbf{y}}}\mu_{\hat{\mathbf{y}}}\right|^2 \sin(\theta)\sin(\beta)\,d\psi\,d\beta\,d\phi\,d\theta \quad [1]$$

$$P = \int_0^{\theta}\int_0^{2\pi}\int_0^{\pi}\int_0^{2\pi} Q_{\perp}\left|E_{\hat{\mathbf{z}}}\mu_{\hat{\mathbf{z}}}\right|^2 \sin(\theta)\sin(\beta)\,d\psi\,d\beta\,d\phi\,d\theta \quad [2]$$

where $\mu_{\hat{\mathbf{y}}}$ and $\mu_{\hat{\mathbf{z}}}$ are the components of the excitation dipole in $\hat{\mathbf{y}}$ and $\hat{\mathbf{z}}$ with respect to positon on the bud surface, $E_{\hat{\mathbf{y}}}$ and $E_{\hat{\mathbf{z}}}$ are the excitation electric field components in $\hat{\mathbf{y}}$ and $\hat{\mathbf{z}}$, and $Q_{\parallel}$ and $Q_{\perp}$ are the light collection efficiencies of the microscope objective for dipoles parallel and perpendicular to the glass surface. The excitation field intensity in $\hat{\mathbf{y}}$ and $\hat{\mathbf{z}}$ were assumed to be the same, though this was an approximation since in reality $\hat{\mathbf{p}}$ had a small component of $\hat{\mathbf{s}}$ (Sund et al., 1999). In addition, in TIR the excitation field decayed exponentially with distance from the glass surface, $E_{\hat{\mathbf{y}}\text{ or }\hat{\mathbf{z}}} = Ee^{-z/2d} = Ee^{-(1-\cos(\theta))/2d}$ where the characteristic decay constant d was defined in terms of a fraction of the radius of the VLP. The collection efficiency for emission parallel $Q_{\parallel}$ versus perpendicular $Q_{\perp}$ were also assumed to be the same ($Q_{\parallel} = Q_{\perp}$), which was an approximation based on the use of a high numerical aperture objective (Anantharam et al., 2010). From coordinate transforms described previously (Anantharam et al., 2010; Sund et al., 1999) the components of the dipoles in $\hat{\mathbf{y}}$ and $\hat{\mathbf{z}}$ are given by:

$$\mu_{\hat{\mathbf{y}}} = \rho(\beta)[\cos(\theta)\sin(\phi)\sin(\beta)\cos(\psi) + \cos(\phi)\sin(\psi)\sin(\beta) + \sin(\theta)\sin(\phi)\cos(\beta)] \quad [3]$$

$$\mu_{\hat{\mathbf{z}}} = \rho(\beta)[-\sin(\theta)\sin(\beta)\cos(\psi) + \cos(\theta)\cos(\beta)] \quad [4]$$

$P/S_{\mathrm{VLP}}\left(\theta, \rho(\beta)\right)$ was solved computationally (Mathematica, Wolfram) with θ parameterized in terms of normalized surface area (A: $0 \rightarrow 1$) as $\theta = \cos^{-1}(1 - 2A)$. In addition, contribution from fluorescence outside of the puncta was accounted for as follows:

$$P/S\,(A, \rho(A), C_{back}) = \frac{A\cdot P/S_{VLP}(A,\rho(A)) + C_{back}\cdot P/S_{Background}}{A + C_{back}} \quad [5]$$

where C_{back} was the background intensity relative to final VLP intensity and $P/S_{Background}$ was the ratio of fluorescence when puncta $A = 0$, i.e. $P/S_{Background} = P/S_{VLP}(0, \rho(0))$.

We found an angle $\beta = 45^{\circ}$, $C_{back} = 0.45$, and $d = 1$ approximately replicated the observed results (Figure 4A,F), reproducing the $t_{1/2\text{ of }P+2S} - t_{1/2\text{ of }P/S}$ of 0.16 (normalized time) (Figure 4B). In Figure 4A an exponential fit to $P + 2S$ was assumed in order to directly equate the VLP area to the predicted P/S. Similar results were obtained by using a uniform distribution of dipoles over an angular range, such as β between 0° to 68.5° or 20° to 63.5°. Thus, our observation is consistent with formation of a spherical bud throughout the recruitment and multimerization of Gag (Carlson et al., 2008; Woodward et al., 2015) which occurs many minutes before recruitment of ESCRT-IIIs.

Discussion

In retroviral assembly, the late domains of Gag are believed to indirectly recruit ESCRT-IIIs which then polymerize into ring or spiral structures at the bud neck to drive bending and scission of the neck membrane (Cashikar et al., 2014; Fabrikant et al., 2009; Hanson et al., 2008). However, our observations compel a new formulation of the role of ESCRTs in bending and scission. First, the initial bending of the membrane from a flat sheet to a spherical bud occurs during Gag assembly and prior to the arrival of ESCRT-IIIs. Thus, ESCRT-IIIs are not required to initiate curvature, a process which may be encouraged by Gag multimerization (Briggs et al., 2009; Wright et al., 2007). Second, the ESCRT-IIIs are only recruited after the accumulation of Gag is complete, indicating that Gag is not sufficient for recruitment. Third, the ESCRT-III/VPS4 are only recruited for tens of seconds and can no longer be detected at the moment of scission. While the ESCRTs and VPS4 cannot be detected in the tens of seconds prior to scission, it does not eliminate the possibility that a subpopulation of fewer than 20% of the ESCRT-III/VPS4, which are not detectable in the background fluctuations, stay around for a longer period of time (further discussed in Materials and Methods).

Factors beyond the late domains which might assist ESCRT-III recruitment include activation through ubiquitination or phosphorylation of Gag or one of the early ESCRTs, such as TSG101 which is co-recruited along with Gag (Bleck et al., 2014; Jouvenet et al., 2011). Additionally, ESCRT-III recruitment might be facilitated by high curvature in the neck or specific lipids recruited to these regions (Lee et al., 2015). The observation that the bulk of measured curvature of the nascent virion occurs prior to the recruitment of ESCRT-IIIs does not rule out any role for ESCRTs in membrane curvature. Indeed, the transient recruitment of ESCRT-IIIs may further constrict the neck linking the virion to the cell to prepare it for scission. The ESCRT-IIIs might facilitate scission by polymerizing into a spiral structure to constrict the neck (‘polymerization constriction’) (Cashikar et al., 2014; Wollert et al., 2009) or into a ring which when removed constricts the neck (‘purse string constriction’, Figure 5) (Saksena et al., 2009). The VPS4 may remove the ESCRT-IIIs potentially acting as a unfoldase (Yang et al., 2015). VPS4 may also remodel the ESCRT-IIIs throughout polymerization, potentially rearranging or tightening the structure (Cashikar et al., 2014). Remodeling is consistent with our observation that recruitment of VPS4 was virtually contemporaneous with the ESCRT-III, with a slight 5 s lag in HEK293T cells and 10 s in HeLa cells (Bleck et al., 2014).

We suggest that fission can only occur when the neck is narrow and after the ESCRT-IIIs are removed (Figure 5). What is driving the scission event if ESCRT-IIIs are gone? When the neck is sufficiently narrow (a few nm) fission may be a spontaneous event, possibly through a hemifission intermediate (Fabrikant et al., 2009; Kozlovsky and Kozlov, 2003). Narrowing of the neck by ESCRT-IIIs may allow additional Gag molecules adjacent to the neck to oligomerize, thereby keeping the constricted structure stable while the ESCRTs are displaced. However, cryo-EM images indicate a gap in the Gag lattice might be present at the site of the neck (Carlson et al., 2008). Alternatively, constriction might encourage exchange or modification of phospholipids with shapes and charges that help to retain a narrow neck following ESCRT-III disappearance. The ESCRT-III are dependent on phospholipids with negative charges. This could explain the greater than 3-fold increased scission rate at a lower pH (10% pCO_2), which would raise the proton concentration to that of the PKa (6.5 and 7.7) (van Paridon et al., 1986), thereby reducing the surface charges (Figure 2F). If scission does not occur sufficiently soon

after removal of ESCRT-IIIs, a new round of ESCRT-III recruitment and assembly is required to achieve scission (Figure 3).

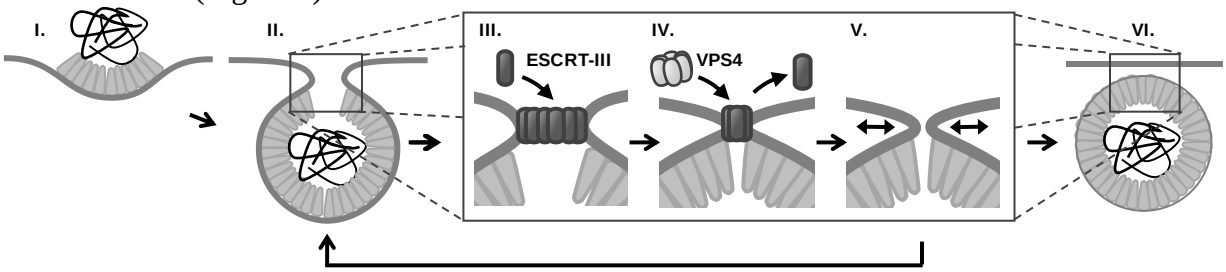

Figure 5. Proposed temporal model of ESCRT-III mediated scission of HIV from cell plasma membrane. (I) The viral particle structure changes throughout accumulation of Gag until (II) a spherical topology prevents incorporation of additional Gags. (III) ESCRT-IIIs (examples: CHMP2, CHMP4) are recruited to the neck and polymerize, with (IV) removal by VPS4 resulting in constriction of the neck. (V) After removal of all ESCRT-IIIs the narrow neck undergoes spontaneous fission, (VI) freeing the virus. If membrane fission does not occur a new round of ESCRT-III recruitment is required (V→ II).

Materials and Methods

Plasmid Construction. Plasmids Gag-mEGFP, Gag-mTagBFP, pLNCX2-mEGFP-VPS4A and pLNCX2-mCherry-CHMP4B were described in Bleck et al. (Bleck et al., 2014) and the plasmids pCR3.1/Syn-Gag and pCR3.1/Syn-Gag-pHluorin were described in Jouvenet et al. (Jouvenet et al., 2008).

pLNCX2-mCherry-CHMP2A-siRNAres and pLNCX2-mCherry-CHMP2B-siRNAres were generated as follows. CHMP2A and CHMP2B were PCR amplified (Platinum PCR SuperMix, Thermo Fisher) from a cDNA library created from HEK293T cells (made via Invitrogen SuperScript III CellDirect kit #46-6320). PCR primers for CHMP2A (NM_014453.3) were 5'-GCGCTCCGGACTCAGATCCCCGGAATTCATGGACCTATTGTTCGGGCG-3' and 5'-GCGCCTCGAGTCAGTCCCTCCGCAGGTTCT-3' and primers for CHMP2B (NM_014043.3) were 5'-GCGCTCCGGACTCAGATCCCCGGAATTCATGGCGTCCCTCTT CAAGAA-3' and 5'-GCGCCTCGAGCTAATCTACTCCTAAAGCCT-3'. After PCR amplification, the fragments were digested with XhoI and BspEI (New England BioLabs, Ipswich, MA) and ligated into the plasmid pLNCX2-mCherry-CHMP4B (which was first digested with the same restriction enzymes to remove CHMP4B) using T4 DNA Ligase (New England BioLabs) yielding the plasmids pLNCX2-mCherry-CHMP2A and pLNCX2-mCherry-CHMP2B. Six silent coding mutations were then incorporated into these plasmids (QuickChange Lightning Site-Directed Mutagenesis Kit, Agilent, Santa Clara, CA) to make them insensitive to siRNA knockdown targeted at the cellular CHMP2A and CHMP2B RNA. The primers for the CHMP2A site-directed mutagenesis were 5'-ACCTGGGACACCACAGCATCGCTTTCTTCCTCGTCCTCCTCATCACCCATGGCATC-3' and 5'-GATGCCATGGGTGATGAGGAGGACGAGGAAGAAAGCGATGCTGTGGTGTC CCAGGT-3' and for CHMP2B were 5'-AACCGTGGATGATGTAATAAAGGAGCAAAACC GTGAATTACGAGGTACACAGAGGGCTAT-3' and 5'-ATAGCCCTCTGTGTACCTCGTA ATTCACGGTTTTGCTCCTTTATTACATCATCCACGGTT-3'. The siRNA sequence for CHMP2A knockdown was 5'-rArArGrArUrGrArArGrArGrGrArGrArGrUrGrAdT

dT-3' (begins at position 464 in NM_014453.2) and for CHMP2B was 5'-rGrGrArArCrArGrAr ArUrCrGrArGrArGrUrUrAdTdT-3' (begins at position 45 in NM_014043.3) (Morita et al., 2011). All ssDNA and ssRNA oligos were purchased from Integrated DNA Technologies (Coralville, IA) and manufacturers' protocols were used for all preparations.

pLNCX2-mEGFP-CHMP2A and pLNCX2-mEGFP-CHMP2B were generated by replacing mCherry in pLNCX-mCherry-CHMP2A and pLNCX-mCherry-CHMP2B with monomeric variant (A206K) of mEGFP from pEGFP-N1 (Clontech/Takara Bio USA, Mountain View, CA). Restriction enzymes AgeI and BspEI (New England BioLabs) were used to digest the backbone and fragments, and these fragments were then ligated into the backbones with T4 DNA ligase. The clonal HeLa cell lines were generated from these plasmids using a previously described protocol (Bleck et al., 2014). pLNCX2-mCherry-VPS4A was generated by replacing mEGFP in pLNCX2-mCherry-VPS4A (Bleck et al., 2014) with mCherry. mCherry was PCR amplified from pmCherry-N1 (Clontech) using In-Fusion recombination primers 5'-CTCTAGCGCTACCGGTCGCCACCATGGTGAGCAAGGGC-3' and 5'-CTCTAGCGCTACCGGTCGCCACCATGGTGAGCAAGGGC-3'. pLNCX2-mEGFP-VPS4A was digested with AgeI and BspEI and the fragment containing VPS4A was gel purified (Thermo Fisher PureLink Quick Gel Extraction Kit). The PCR product was then inserted into purified backbone using In-Fusion HD Cloning Kit (Clontech) according to manufacturer's instructions.

Gag-MA-sf3 and Gag-MA-sf11 were generated by inserting the circularly permuted superfolder GFPs (provided by Jeffrey Waldo lab) (Pedelacq et al., 2006) into a variant of pCR3.1/Syn-Gag that has an EcoRV restriction enzyme site near the carboxy terminal of MA (Asn-Gln-Val-Ser modified to Asn-Gln-**Asp**-**Ile**-Val-Ser). Circularly permuted version 3 was PCR amplified with recombination In-Fusion primers 5'-CACAGCAACCAGGATGGCAGCAGCCATCATCATC-3' and 5'-GTTCTGGCTGACGATGGTACCTCCAGTAGTGCAAATAA-3'. The primers for circularly permuted version 11 were 5'-CACAGCAACCAGGATGGCAGCAGCCATCATCAT C-3' and 5'-GTTCTGGCTGACGATGGTACCATCTTCAATGTTGTGG-3'. After digesting pCR3.1/Syn-Gag-EcoRV with EcoRV (New England BioLabs) the In-Fusion HD kit was used to insert PCR fragments into the Syn-Gag backbone.

Sample Preparation. With the exception of 120 s pCO_2 switching data, all imaging was conducted in HEK293T cells grown in DMEM (#11965, Thermo Fisher Scientific, Waltham, MA) with 10% FBS (#F4135, MilliporeSigma, St. Louis, MO). HEK293T cells were gift from P. Bianiaz Laboratory and were not been authenticated or tested for mycoplasma contamination. 120 s pCO_2 switching experiments imaged in HeLa cells which were grown in the same growth medium. HeLa cells were from ATCC and were not authenticated or tested for mycoplasma contamination. For polarization excitation experiments cells were grown on 35 mm glass bottom dishes (#P35G-1.0-20-C, MatTek, Ashland, MA) coated with fibronectin (#33010, Thermo Fisher) by incubating the dish with 10 µg/ml fibronectin in PBS for 1 hour. For pCO_2 switching experiments perfusion slides (#80186 µ-Slide, Ibidi, Martinsried, Germany) were incubated with 60 µg/ml fibronectin in PBS for 1 hour before plating cells. For all experiments cells at ~75% confluency were transfected with expression plasmids ~3.5 hours prior to beginning to image. For transfection 8 µl of Lipofectamine2000 (#11668, Thermo Fisher) was incubated for 5 min in 250 µl of Opti-MEM I (#31985, Thermo Fisher) and 2000 µg of DNA was incubated for 5 min in 250 µl of Opti-MEM I. Both solutions were then mixed and incubated for 20 minutes before

adding to adhered cells on MatTek dish in 2000 µl of DMEM. The same procedure was used for cells in the flow slide, but the transfection mixture was added to 2000 µl of DMEM and then 1000 µl was perfused through the chamber. At least four cells were used for each experimental condition in order to account for potential variability between cells. Both CHMP2A and CHMP2B were knocked down with siRNA for mCherry-CHMP2A and mCherry-CHMP2B experiments. siRNA transfections were conducted 48 hours prior to DNA plasmid transfection using Lipofectamine RNAiMAX (following manufacturer's instructions; #13778, Thermo Fisher). A second round of siRNA transfection was performed at the time of DNA transfection. The following DNA ratios were used for transfections: Gag:Gag-mEGFP (4:1), Gag:Gag-MA-sf3 (4:1), Gag:Gag-MA-sf3 (4:1), Gag:Gag-pHluorin:mCherry-VPS4A (12:3:5), Gag:Gag-pHluorin:mCherry-CHMP4B (12:3:5), Gag:Gag-pHluorin:mCherry-CHMP2A-siRNAres (4:1:5), Gag:Gag-pHluorin:mCherry-CHMP2B-siRNAres (4:1:5), Gag:Gag-TagBFP:mEGFP-VPS4A:mCherry-CHMP4B (24:6:5:5). Note: The Gag to tagged Gag ratio was 4:1 in all experiments.

CO_2 modulation system. Gas from compressed cylinders was bubbled into two imaging media reservoirs (140 ml open piston Monoject syringe, Medtronic, Minneapolis, MN) partially filled with cell imaging media (10 mM HEPES, 9.7 g/L of Hanks BBS (MilliporeSigma), and NaOH to adjust the pH to 7.4) with 1% FBS. One reservoir was equilibrated with compressed air (labeled 0% in these experiments but actually contained 0.04% CO_2), and the other reservoir was equilibrated with 10% CO_2 (balanced with air) (Figure 1 – figure supplement 1). The reservoirs were mounted to a flow perfusion system (ValveBank II, AutoMate Scientific, Berkeley, CA) which enabled automated selection of desired media via solenoid valves under the reservoirs. Tygon tubes (R-3603) from each valve carried the media to a fluid combiner just prior to the perfusion slide chamber containing adhered cells. After the flow chamber a single tube carried the discharge media to a collection container. This container was placed below the height of equilibration reservoirs so that fluid flow was driven by gravity. The flow rate (~ 3 ml/min) was controlled with a clamp regulator attached to the discharge tube. At this flow rate the response time of the fluorophores to a pCO_2 change, characterized in terms of an exponential decay constant, was ~ 7 s. A peristaltic pump (MS-Reglo, Ismatec/Cole-Parmer, Wertheim, Germany) then passed the media from the collection reservoir back to the equilibration reservoirs so that the media could be recycled. The microscope and entire imaging media flow system were enclosed in a temperature control box held at 37°C. Valve regulation, camera trigger and laser excitation were all controlled via custom software written in LabView (National Instruments, Austin, TX).

Imaging with pCO_2 switching. For experiments with pCO_2 switching every 10 s the media was continuously flowed through the imaging chamber, with the reservoir supplying the media being switched every 10 s. Two images were collected every 2.5 s (4.0 s for CHMP4B experiments) with 488nm excitation for pHluorin (100 ms exposure with power between 1-5 mW), followed by 594 nm excitation for mCherry (100 ms exposure with laser power between 5-20 mW; 100mW DPSS laser, Cobolt, Solna, Sweden). A multipass emission filter (zet405/488/594m, Chroma Technology, Bellows Falls, VT) enabled rapid sequential wavelength imaging. For experiments with pCO_2 switching every 120 s the desired media was only applied to the chamber for 10s, followed by no flow for 110 s. During this time sequential 488 nm (100 ms, 1 mW) and 594 nm (100 ms, 1 mW) excitation images were captured every 10 s. All experiments were conducted with 100 Hz azimuthal scanning TIR-FM illumination.

Temporal determination of scission. The cytosolic pH was oscillated by switching the pCO_2 from 0% to 10% (for an average of 5%) every 10 seconds or every 120 s. The cytosolic carbonic anhydrase ensures that the pH in the cytosol closely tracks the pCO_2 (Simon et al., 1994). At scission the luminal pH of the VLP or virion is no longer continuous with the cytosol and no longer tracks the cytosolic pH. Individual VLPs were identified from the Gag-pHluorin images using Metamorph (version 7.8.10, Molecular Devices, Sunnyvale, CA) and the peak pixel amplitude in a 15 pixel (975 nm) diameter regions of interests centered on individual VLPs was found for all frames (Figure 1, Figure 1 – figure supplement 2).

For switching every 10 s we used a custom LabView software lock-in amplifier to find changes in VLP sensitivity to pCO_2 modulation. The data were high-pass filtered (2-pole Butterworth with 0.01 Hz cutoff) to bias the pCO_2 dependent pHluorin intensity fluctuations (with a period of 20s) around 0. This signal was then multiplied by an in-phase sine wave with the same period and a moving average was calculated over a period of 60 s. A significant change in signal indicated a change in sensitivity to pCO_2 modulation. At many of the identified VLPs a clear transition from a high plateau to a low plateau in the lock-in signal was observed (Figure 1 – figure supplement 2). The moment of scission was classified as the halfway amplitude between the two plateaus, with half of the moving window containing pre-scission data and the other half containing post-scission data (Figure 1 – figure supplement 2A). In the same regions of interest the average mCherry signal (tagged to VPS4A, CHMP4B, CHMP2A, or CHMP2B) was analyzed and peaks were identified in which there was a clear increase followed by decrease in fluorescence intensity (Figure 1A,C,E,G and Figure 1 – figure supplement 2). The appearance time was identified when a signal was first observed above cellular background, and the disappearance time when the signal dropped to cellular background. Appearance and disappearance relative to scission were then found by comparing these times to the scission time (Figure 1B,D,F,H). Based on the observed distribution of appearance and disappearance times relative to scission, with an average of roughly a minute, we excluded data in which scission and ESCRT-III/VPS4A recruitment were more than four minutes apart. Excluded data was attribute to a failed or uncorrelated scission event. ~25 traces under each condition were collected to gain understanding of the distribution of events.

The average signal-to-noise was approximately 7:1 (peak signal:S.D.) across all ESCRT-III/VPS4A measurements, and ESCRT-III/VPS4A recruitment was estimated to be detectable when the sustained signal deviated from the mean by ~1-2 standard deviations. Based on this deviation it is estimated that ESCRT-III/VPS4A recruitment below ~20% of peak recruitment would be undetected. We estimate that there are between 10-100 ESCRTs in a complex at peak signal, with the possibility of < 10 ESCRTS undetectable in the background noise. Assuming a peak signal (100 ESCRTs) decreases exponentially into the noise after 10s (10 ESCRTS), we estimate only ~1 ESCRTs would remain after another 10s. This time is comparable to the ~20s measured between peak disappearance and scission. If the disappearance is faster than exponential, e.g. linear, the ESCRTs will be gone even sooner. This interpolation of ESCRT-IIIs or VPS4A disappearance profiles into the noise indicates the ESCRTs predominantly leave the budding site prior to scission (Figure 1 – figure supplement 2). For a significant number (> 1) of either ESCRT-IIIs or VPS4A to be around following scission there would need to be a second, smaller population that follows much slower disappearance kinetics.

For pCO_2 switching every 120 s for each tracing we determined the first transition of pCO_2 for which the fluorescence had decreased sensitivity, indicating protons were no long

freely flowing between cytosol and lumen of the VLP. We assumed that scission must have occurred during the previous plateau of pCO_2 (Figure 2A-E). For example, if scission occurred during the 10% pCO_2 cycle (low fluorescence) then after the next transition to 0% pCO_2, and all subsequent transitions, the fluorescence would be closer to that of the 10% (low fluorescence state than the 0% pCO_2 (high fluorescence) state. Conversely, if scission occurred during the 0% (high fluorescence), future 10% pCO_2 plateaus would be closer to the high fluorescence state. Occasionally traces appeared to be trapped in an intermediate pH state, which we attribute to scission occurring during the transition between pCO_2 states. Individual VLP traces were categorized into being trapped in a high, middle or low pH state by comparing the Gag-pHLuorin signal before and after the VLP became insensitive to pCO_2 switching (Figure 2F).

Simultaneous VPS4A and CHMP4B imaging. Gag-mTagBFP, mEGFP-VPS4A and mCherry-CHMP4B were imaged in TIRFM with sequential illumination of 594 nm (100ms, 10-20 mW), 488 nm (100ms, 4-10mW) and 405 nm (100ms, 2-4mW; 120 mW LuxX diode laser, Omicron). mEGFP-VPS4A and mCherry-CHMP4B images were acquired every 5 s and Gag-TagBFP images were acquired every 60 s. VPS4A and CHMP4B relative appearance time were conducted using the same method as described previously (Figure 1 – figure supplement 4) (Bleck et al., 2014).

mEGFP-CHMP2A/B knockdown imaging. HeLa cell lines stably expressing either mEGFP-CHMP2A or mEGFP-CHMP2B and transfected with the respective siRNA (48hrs in advance) were imaged on an inverted microscope (IX-70, Olympus, Shinjuku, Japan) with epi-illumination via a Xenon lamp and transmitted bright-field illumination (Figure 1 – figure supplement 3).

Polarized excitation imaging. Images were collected on an inverted microscope (IX-81, Olympus) with a custom built through-the-objective (100X UAPON 1.49 NA, Olympus) polarized TIRFM illuminator (Johnson et al., 2014). Throughout imaging the excitation TIR light was azimuthally scanned at 200 Hz with mirror galvanometers (Nutfield Technology, Hudson, NH) in order to reduce spatial illumination nonuniformities. A multiband polychroic (zt405/488/594/647rpc 2mm substrate, Chroma) was positioned between the galvanometers and objective in order to isolate the excitation light from the emitted light. Light from a 488nm laser (100 mW LuxX diode laser, Omicron, Rodgau-Dudenhofen, Germany) was modulated between being polarized perpendicular ($\hat{\mathbf{p}}$) or parallel ($\hat{\mathbf{s}}$) to the glass surface by passing the light through an EOM (Conoptics, Danbury, CT) and quarter-wave plate prior to the galvanometer scan-head. The polarization generated by the EOM was modulated in sync with the galvanometers such that during scanning a $\hat{\mathbf{p}}$ or $\hat{\mathbf{s}}$ state was maintained at all azimuthal positions. The scanning polar angle was selected such that the excitation light was just beyond the TIR critical angle, minimizing $\hat{\mathbf{s}}$ polarized light contaminating $\hat{\mathbf{p}}$ excitation(Johnson et al., 2014).

A combined $\hat{\mathbf{p}}/\hat{\mathbf{s}}$ ratio image was collected every 30s. To generate this ratio image a sequential series of 10 $\hat{\mathbf{p}}$ and $\hat{\mathbf{s}}$ images were collected, divided (after subtracting camera offset), and then averaged. Each $\hat{\mathbf{p}}$ or $\hat{\mathbf{s}}$ image had an exposure of 5 ms (laser power between 25-50mW), with a new image collected every 15 ms. Thus, in 30 ms a single $\hat{\mathbf{p}}/\hat{\mathbf{s}}$ image was generated, and then 10 of these images (over a 300 ms duration) were averaged (ImageJ) (Schneider et al., 2012) to create the combined ratio image. The short period was utilized in order to minimize artifacts in the $\hat{\mathbf{p}}/\hat{\mathbf{s}}$ ratio image from VLP or cell movement. The galvonometers, EOM, camera shutter, and laser shutters were all driven/triggered by a multifunction data acquisition board (PCIe-6323, National Instruments) and controlled from custom written software in LabView. Images were

streamed from a CMOS camera (Flash-4.0, Hamamatsu, Hamamatsu City, Japan) to a workstation (T7500, Dell, Round Rock, TX) running image acquisition software (Metamorph). A single band emission filter (ET525/50m, Chroma) was used to isolate fluorophore emission. In order to characterize the amount of Gag in an assembling VLP, an average $\hat{\mathbf{p}} + 2 \cdot \hat{\mathbf{s}}$ image was also generated at each time point.

Polarization Analysis. Puncta were found in the $\hat{\mathbf{p}} + 2 \cdot \hat{\mathbf{s}}$ images which increased and then plateaued in amplitude. These puncta were then selected for orientation analysis with $\hat{\mathbf{p}}/\hat{\mathbf{s}}$. A 2D Gaussian was fit to these assembling puncta to find a frame by frame subpixel peak location. Using bilinear interpolation the $\hat{\mathbf{p}}/\hat{\mathbf{s}}$ and $\hat{\mathbf{p}} + 2 \cdot \hat{\mathbf{s}}$ images were resampled 10X in the horizontal and vertical directions (65 nm to 6.5 nm wide pixels). On these resampled images P/S and P + 2S values were found by averaging the resampled pixel intensities that are within 100nm of the peak fit locations (Figure 4A, Figure 4 – figure supplement 1). For frames prior to the appearance of a puncta P/S and P + 2S values were determined using the fit location of the first frame in which there was a puncta fit. For each tagged version of Gag the average P/S value for background and assembled VLPs was calculated by finding an average P/S for each trace before assembly and after a plateau was reached, and then averaging across all traces (Figure 4B). A relative time to half growth for each VLP was determined by finding the halfway to assembly point (i.e. the point where the intensity is halfway between the intensity at assembly beginning and plateau) and then finding the normalized time at this point relative to the time assembly began and appeared to reach a plateau. This normalized time was between 0 and 1. A normalized time to halfway drop in P/S was also found (normalized to the same time scale) and these values were subtracted to find: $t_{1/2 \text{ of P+2S}} - t_{1/2 \text{ of P/S}}$ (normalized). All fluorophore combinations were included in the P/S histogram (Figure 4C) since all combinations had similar P/S characteristics.

Acknowledgements

We thank M. Will and M. A. Lockard for assisting with plasmid preparations. We also thank M. S. Itano, M. D. Tomasini, K. Bredbenner and P. Bieniasz for discussion during manuscript preparation. This work was supported by NIH grants 1P50GM103297 and R01 GM11958 to S.M.S.

Author Contributions

D.S.J., M.B., and S.M.S. designed experiments. D.S.J. and M.B. prepared samples. D.S.J. collected and analyzed data. D.S.J., M.B., and S.M.S. wrote manuscript.

Competing interests: The authors declare that no competing interests exist.

References

Anantharam, A., B. Onoa, R.H. Edwards, R.W. Holz, and D. Axelrod. 2010. Localized topological changes of the plasma membrane upon exocytosis visualized by polarized TIRFM. *The Journal of cell biology*. 188:415-428.

Babst, M., D.J. Katzmann, E.J. Estepa-Sabal, T. Meerloo, and S.D. Emr. 2002a. Escrt-III: an endosome-associated heterooligomeric protein complex required for mvb sorting. *Developmental cell*. 3:271-282.

Babst, M., D.J. Katzmann, W.B. Snyder, B. Wendland, and S.D. Emr. 2002b. Endosome-associated complex, ESCRT-II, recruits transport machinery for protein sorting at the multivesicular body. *Developmental cell*. 3:283-289.

Baumgartel, V., S. Ivanchenko, A. Dupont, M. Sergeev, P.W. Wiseman, H.G. Krausslich, C. Brauchle, B. Muller, and D.C. Lamb. 2011. Live-cell visualization of dynamics of HIV budding site interactions with an ESCRT component. *Nature cell biology*. 13:469-474.

Bleck, M., M.S. Itano, D.S. Johnson, V.K. Thomas, A.J. North, P.D. Bieniasz, and S.M. Simon. 2014. Temporal and spatial organization of ESCRT protein recruitment during HIV-1 budding. *Proceedings of the National Academy of Sciences*. 111:12211-12216.

Briggs, J.A., J.D. Riches, B. Glass, V. Bartonova, G. Zanetti, and H.G. Krausslich. 2009. Structure and assembly of immature HIV. *Proceedings of the National Academy of Sciences of the United States of America*. 106:11090-11095.

Carlson, L.A., J.A. Briggs, B. Glass, J.D. Riches, M.N. Simon, M.C. Johnson, B. Muller, K. Grunewald, and H.G. Krausslich. 2008. Three-dimensional analysis of budding sites and released virus suggests a revised model for HIV-1 morphogenesis. *Cell host & microbe*. 4:592-599.

Cashikar, A.G., S. Shim, R. Roth, M.R. Maldazys, J.E. Heuser, and P.I. Hanson. 2014. Structure of cellular ESCRT-III spirals and their relationship to HIV budding. *eLife*. 3.

Chiaruttini, N., L. Redondo-Morata, A. Colom, F. Humbert, M. Lenz, S. Scheuring, and A. Roux. 2015. Relaxation of Loaded ESCRT-III Spiral Springs Drives Membrane Deformation. *Cell*. 163:866-879.

Dobro, M.J., R.Y. Samson, Z. Yu, J. McCullough, H.J. Ding, P.L. Chong, S.D. Bell, and G.J. Jensen. 2013. Electron cryotomography of ESCRT assemblies and dividing Sulfolobus cells suggests that spiraling filaments are involved in membrane scission. *Molecular biology of the cell*. 24:2319-2327.

Fabrikant, G., S. Lata, J.D. Riches, J.A. Briggs, W. Weissenhorn, and M.M. Kozlov. 2009. Computational model of membrane fission catalyzed by ESCRT-III. *PLoS Comput Biol*. 5:e1000575.

Hanson, P.I., R. Roth, Y. Lin, and J.E. Heuser. 2008. Plasma membrane deformation by circular arrays of ESCRT-III protein filaments. *The Journal of cell biology*. 180:389-402.

Henne, W.M., N.J. Buchkovich, Y. Zhao, and S.D. Emr. 2012. The endosomal sorting complex ESCRT-II mediates the assembly and architecture of ESCRT-III helices. *Cell*. 151:356-371.

Henne, W.M., H. Stenmark, and S.D. Emr. 2013. Molecular mechanisms of the membrane sculpting ESCRT pathway. *Cold Spring Harb Perspect Biol*. 5.

Hulikova, A., and P. Swietach. 2014. Rapid CO2 permeation across biological membranes: implications for CO2 venting from tissue. *FASEB journal : official publication of the Federation of American Societies for Experimental Biology*. 28:2762-2774.

Hurley, J.H. 2015. ESCRTs are everywhere. *The EMBO journal*. 34:2398-2407.

Ivanchenko, S., W.J. Godinez, M. Lampe, H.G. Krausslich, R. Eils, K. Rohr, C. Brauchle, B. Muller, and D.C. Lamb. 2009. Dynamics of HIV-1 assembly and release. *PLoS Pathog*. 5:e1000652.

Johnson, D.S., R. Toledo-Crow, A.L. Mattheyses, and S.M. Simon. 2014. Polarization-controlled TIRFM with focal drift and spatial field intensity correction. *Biophysical journal*. 106:1008-1019.

Jouvenet, N., P.D. Bieniasz, and S.M. Simon. 2008. Imaging the biogenesis of individual HIV-1 virions in live cells. *Nature*. 454:236-240.

Jouvenet, N., S.M. Simon, and P.D. Bieniasz. 2009. Imaging the interaction of HIV-1 genomes and Gag during assembly of individual viral particles. *Proceedings of the National Academy of Sciences of the United States of America*. 106:19114-19119.

Jouvenet, N., M. Zhadina, P.D. Bieniasz, and S.M. Simon. 2011. Dynamics of ESCRT protein recruitment during retroviral assembly. *Nature cell biology*. 13:394-401.

Katzmann, D.J., M. Babst, and S.D. Emr. 2001. Ubiquitin-dependent sorting into the multivesicular body pathway requires the function of a conserved endosomal protein sorting complex, ESCRT-I. *Cell*. 106:145-155.

Katzmann, D.J., C.J. Stefan, M. Babst, and S.D. Emr. 2003. Vps27 recruits ESCRT machinery to endosomes during MVB sorting. *The Journal of cell biology*. 162:413-423.

Kooijman, E.E., K.E. King, M. Gangoda, and A. Gericke. 2009. Ionization properties of phosphatidylinositol polyphosphates in mixed model membranes. *Biochemistry*. 48:9360-9371.

Kozlovsky, Y., and M.M. Kozlov. 2003. Membrane fission: model for intermediate structures. *Biophysical journal*. 85:85-96.

Lata, S., G. Schoehn, A. Jain, R. Pires, J. Piehler, H.G. Gottlinger, and W. Weissenhorn. 2008. Helical structures of ESCRT-III are disassembled by VPS4. *Science*. 321:1354-1357.

Lee, I.H., H. Kai, L.A. Carlson, J.T. Groves, and J.H. Hurley. 2015. Negative membrane curvature catalyzes nucleation of endosomal sorting complex required for transport (ESCRT)-III assembly. *Proceedings of the National Academy of Sciences of the United States of America*. 112:15892-15897.

Martin-Serrano, J., A. Yarovoy, D. Perez-Caballero, and P.D. Bieniasz. 2003. Divergent retroviral late-budding domains recruit vacuolar protein sorting factors by using alternative adaptor proteins. *Proceedings of the National Academy of Sciences of the United States of America*. 100:12414-12419.

McCullough, J., A.K. Clippinger, N. Talledge, M.L. Skowyra, M.G. Saunders, T.V. Naismith, L.A. Colf, P. Afonine, C. Arthur, W.I. Sundquist, P.I. Hanson, and A. Frost. 2015. Structure and membrane remodeling activity of ESCRT-III helical polymers. *Science*. 350:1548-1551.

Miesenbock, G., D.A. De Angelis, and J.E. Rothman. 1998. Visualizing secretion and synaptic transmission with pH-sensitive green fluorescent proteins. *Nature*. 394:192-195.

Morita, E., L.A. Colf, M.A. Karren, V. Sandrin, C.K. Rodesch, and W.I. Sundquist. 2010. Human ESCRT-III and VPS4 proteins are required for centrosome and spindle maintenance. *Proceedings of the National Academy of Sciences of the United States of America*. 107:12889-12894.

Morita, E., V. Sandrin, J. McCullough, A. Katsuyama, I. Baci Hamilton, and W.I. Sundquist. 2011. ESCRT-III protein requirements for HIV-1 budding. *Cell host & microbe*. 9:235-242.

Muziol, T., E. Pineda-Molina, R.B. Ravelli, A. Zamborlini, Y. Usami, H. Gottlinger, and W. Weissenhorn. 2006. Structural basis for budding by the ESCRT-III factor CHMP3. *Developmental cell*. 10:821-830.

Obita, T., S. Saksena, S. Ghazi-Tabatabai, D.J. Gill, O. Perisic, S.D. Emr, and R.L. Williams. 2007. Structural basis for selective recognition of ESCRT-III by the AAA ATPase Vps4. *Nature*. 449:735-739.

Pedelacq, J.D., S. Cabantous, T. Tran, T.C. Terwilliger, and G.S. Waldo. 2006. Engineering and characterization of a superfolder green fluorescent protein. *Nature biotechnology*. 24:79-88.

Saksena, S., J. Wahlman, D. Teis, A.E. Johnson, and S.D. Emr. 2009. Functional reconstitution of ESCRT-III assembly and disassembly. *Cell*. 136:97-109.

Schneider, C.A., W.S. Rasband, and K.W. Eliceiri. 2012. NIH Image to ImageJ: 25 years of image analysis. *Nature methods*. 9:671-675.

Simon, S., D. Roy, and M. Schindler. 1994. Intracellular pH and the control of multidrug resistance. *Proceedings of the National Academy of Sciences of the United States of America*. 91:1128-1132.

Stuchell-Brereton, M.D., J.J. Skalicky, C. Kieffer, M.A. Karren, S. Ghaffarian, and W.I. Sundquist. 2007. ESCRT-III recognition by VPS4 ATPases. *Nature*. 449:740-744.

Sund, S.E., J.A. Swanson, and D. Axelrod. 1999. Cell membrane orientation visualized by polarized total internal reflection fluorescence. *Biophysical journal*. 77:2266-2283.

van Paridon, P.A., B. de Kruijff, R. Ouwerkerk, and K.W. Wirtz. 1986. Polyphosphoinositides undergo charge neutralization in the physiological pH range: a 31P-NMR study. *Biochim Biophys Acta*. 877:216-219.

Wollert, T., C. Wunder, J. Lippincott-Schwartz, and J.H. Hurley. 2009. Membrane scission by the ESCRT-III complex. *Nature*. 458:172-177.

Woodward, C.L., S.N. Cheng, and G.J. Jensen. 2015. Electron cryotomography studies of maturing HIV-1 particles reveal the assembly pathway of the viral core. *Journal of virology*. 89:1267-1277.

Wright, E.R., J.B. Schooler, H.J. Ding, C. Kieffer, C. Fillmore, W.I. Sundquist, and G.J. Jensen. 2007. Electron cryotomography of immature HIV-1 virions reveals the structure of the CA and SP1 Gag shells. *The EMBO journal*. 26:2218-2226.

Yang, B., G. Stjepanovic, Q. Shen, A. Martin, and J.H. Hurley. 2015. Vps4 disassembles an ESCRT-III filament by global unfolding and processive translocation. *Nature structural & molecular biology*. 22:492-498.